



Elucidation of the mechanistic origin of spin-state-dependent P-doped Fe single-atom catalysts for the oxidation of organic pollutants through peroxymonosulfate activation

Yandong Chai^a, Hongling Dai^a, Xiaoguang Duan^{b,*}, Zhiqiang Sun^c, Fengping Hu^a, Jin Qian^d, Xiaoming Peng^{a,*}

^a School of Civil Engineering and Architecture, East China Jiaotong University, Nanchang 330013, PR China

^b School of Chemical Engineering, The University of Adelaide, Adelaide, SA 5005, Australia

^c State Key Laboratory of Urban Water Resource and Environment, School of Environment, Harbin Institute of Technology, Harbin 150090, PR China

^d School of Chemistry and Chemical Engineering, Northwestern Polytechnical University, Xi'an 710000, PR China

ARTICLE INFO

Keywords:

Electron density
Energy gap
Electronic structure modulation
Electron transfer
DFT calculation

ABSTRACT

In this study, the Fe single-atom catalyst (Fe-NC) was decorated via electronic structure modulation strategy and P was introduced into the second shell layer to improve the ability for peroxymonosulfate (PMS) activation. The Fe-PNC exhibits outstanding activity for bisphenol A (BPA) oxidation ascribed to its unique coordination environment (Fe-N₄P₂) and high spin state in comparison with Fe-NC (Fe-N₄, low spin state) supported by the experimental data and density functional theory (DFT) calculations. We demonstrate that the higher energy of Fe 3d orbitals could better overlap with the O 2p orbitals of PMS, facilitating the electron transfer from Fe sites to PMS. In addition, P doping lowered the splitting field energy of the ligand and the energy gap between the contaminant and the catalyst, accelerating the transfer electrons from the adsorbed contaminant to the Fe site, thus maintaining the high spin state of Fe site and improving the stability of catalysis.

1. Introduction

The Fenton method is one of the most effective water pollution control techniques for addressing pollutants generated by dramatic population growth and rapid expansion of industry and agriculture [1]. Among them, permonosulfate (PMS)-based advanced oxidation processes have been widely reported for their wide applicability in degrading pollutants as well as their safety and stability [2]. However, the mild PMS reaction during oxidation leads to excessive costs and large chemical inputs [3]. Therefore, it is necessary to activate PMS with catalysts to accelerate contaminant degradation. Although transition metal ions (Co²⁺, Fe²⁺, Cu²⁺, and Mn²⁺) usually exhibit significant PMS activation ability, they also suffer from problems such as poor recoverability and sludge accumulation. Non-homogeneous catalysts using various metal nanoparticles (e.g. CuFe₂O₄, Co₃O₄, CuO, MnO₂, and Mn₂O₃) are commonly used to replace homogeneous catalysts [4]. However, the catalytic activity of metal nanoparticles within homogeneous active centers is relatively low.

In the last decade, carbon materials, especially monatomic transition

metal and nitrogen co-doped carbon (M-N-C) materials have been widely used as heterogeneous catalyst for advanced oxidation processes [5–7]. In order to improve atom utilization and catalytic efficiency, scientists have endeavored to reduce the size of catalysts from microns to nanometers to single-atom catalysts [8].

In terms of catalyst miniaturization, scientists have mainly concerned with the size of the material, which is currently relatively well-defined on a theoretical level [9]. However, in the area of peroxymonosulfate (PMS)-AOPs, there are fewer studies on enhancing the catalytic capacity on the atomic scale by regulating the electronic structure of metal centers [10]. Experimental studies have shown that Fe-N₄ sites served as the main active site of Fe-NC catalysts. Nevertheless, the catalytic activity of Fe-N₄ sites on different carbon carriers varies considerably, which is most associated with the intrinsic structure of the carbon carriers, especially the electronic structure [11,12]. Changes in the electronic structure of the carbon carriers simultaneously affect the nature of the electronic structure of the Fe-N₄ sites through interactions [13]. However, the fundamental cause of the change in catalytic activity of Fe-N₄ remains unclear. In several recent studies, it

* Corresponding authors.

E-mail addresses: xiaoguang.duan@adelaide.edu.au (X. Duan), pengxiaoming70@ecjtu.edu.cn (X. Peng).

<https://doi.org/10.1016/j.apcatb.2023.123289>

Received 16 July 2023; Received in revised form 9 September 2023; Accepted 12 September 2023

Available online 14 September 2023

0926-3373/© 2023 Elsevier B.V. All rights reserved.

has been pointed out that the electronic structure (electron absorbing/giving nature) of the carbon carrier affected the d-orbital energy level or d-band center of the Fe sites [14]. However, it has also been suggested that it can modulate the charge state of Fe site thereby affecting its catalytic activity [15]. A great deal of work has been done to reveal the source of the differences in the catalytic performance of Fe-N₄ catalytic activity in order to understand it, but no breakthrough has been achieved.

Adjusting the coordination environment of the metal center by doping the carbon carrier with heteroatoms can effectively tune its electronic structure [16,17]. It has been previously reported that Fe-N₄ sites can be reconfigured to Fe-C₂N₁ sites by acid etching, which can enhance the activation of the catalyst for PMS and lower the energy barrier for the generation of singlet oxygen [18]. In addition, the introduction of electron-deficient or electron-rich nonmetallic heteroatoms (B or P) in monometallic (Fe or Cu) carbon-based materials, for example, can also modulate the electronic structure by changing the electron density or orbital occupation in the metal center [19]. The above strategies are implemented to modulate the valence and spin

states of the metal center by the interaction between the metal center and the dopant element (located in the first or second coordination shell layer).

Therefore, it is reasonable to micromodulate the electronic structure by tuning the three-dimensional electrons to achieve a stronger modulation effect. In the present study, iron-based single atom catalysts were used as a model, and the effect of the introduction of P element on its activation of PMS was evaluated. ZIF-8 was used as a carrier to synthesize loaded target iron catalysts. The P element was introduced to form the "Fe-N₄P₂" structure through ligand reactions and restriction effects. Bisphenol A(BPA) was chosen as a model contaminant to assess the catalyst activity. Finally, The mechanism of P-induced spin state and charge changes of the Fe center to PMS activation is elucidated according to both experiment results and density flooding theory (DFT) calculations.

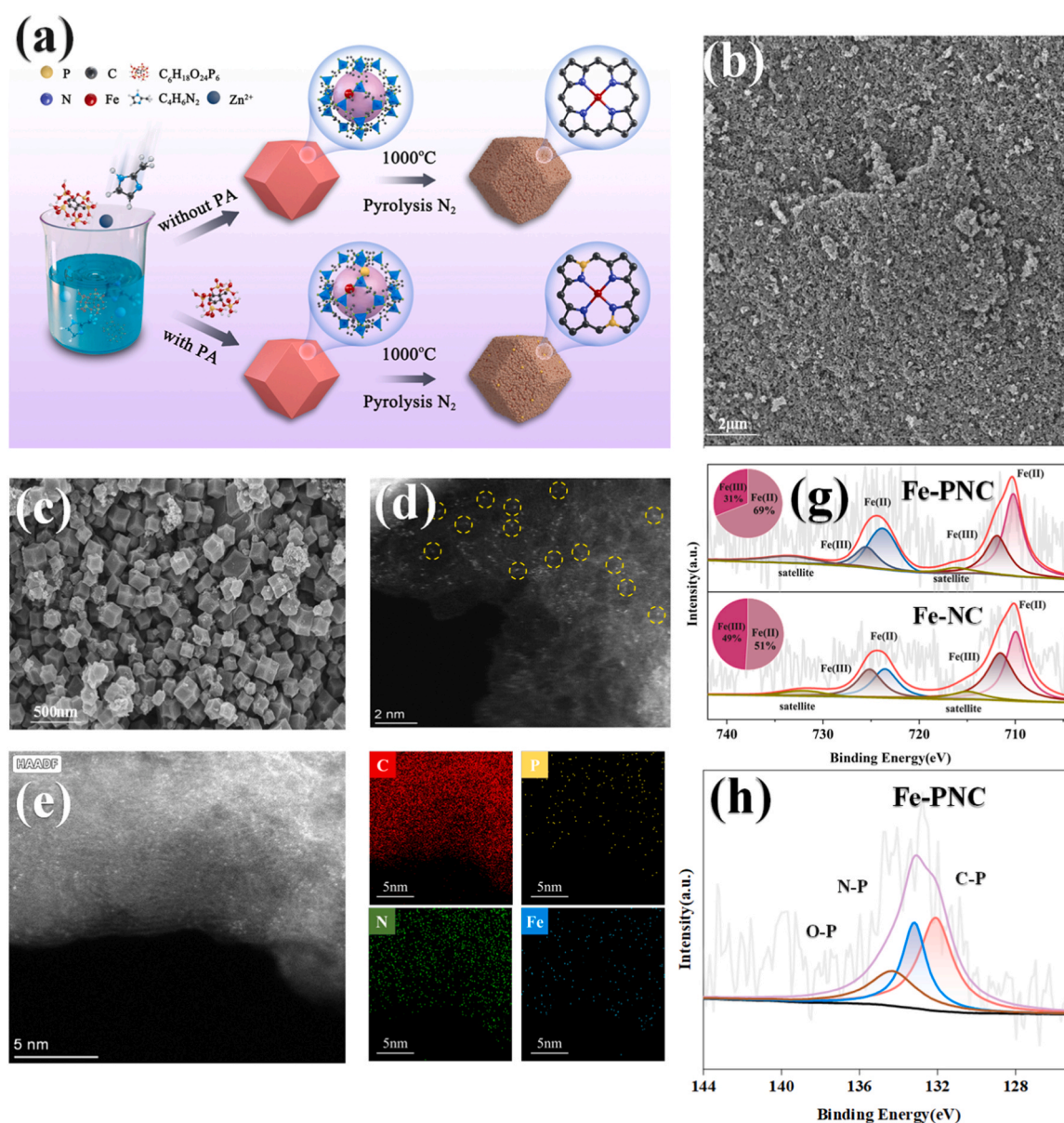


Fig. 1. (a) Steps for the synthesis of the samples; SEM images of Fe-PNC at different scales (b) 2 μm and (c) 500 nm; (d) AC HAADF-STEM images of Fe-PNC; (e) HAADF-HRTEM of Fe-PNC; (f) HRTEM mapping of Fe-PNC; (g) Fe 2p XPS spectrum of Fe-PNC and Fe-NC; (h) P 2p XPS spectrum of Fe-PNC.

2. Experimental section

2.1. Experimental materials

Phytic acid (PA, 50% (w/w) in H₂O), Zinc nitrate hexahydrate (Zn(NO₃)₂·6H₂O), iron nitrate nonahydrate (Fe(NO₃)₃·9H₂O), 2-methylimidazole(2-MeOH), ethanol, potassium peroxysulfate (PMS), bisphenol A (BPA), humic acid (HA), tert-butyl alcohol (TBA), p-benzoquinone (P-BQ), phenol (Phenol), furfuryl alcohol (FFA), sodium nitrate (NaNO₃) are all of the analytical grade. All chemicals were procured from Shanghai Maclean Biochemical Co. The lake water used in this study was taken from Poyang Lake, the sudge water was taken from Shuanggang Water Plant of Nanchang City, and the Cultured wastewater was taken from Liuche Village, Xunwu County, Ganzhou City, China.

2.2. Preparations of catalysts

90 mg of Fe(NO₃)₃·9H₂O and 3.75 g of Zn(NO₃)₂·6H₂O was dispersed in 300 mL methanol. After the solution was heated to 60 °C, 126 µL of phytic acid (PA, 50% (w/w) in H₂O) was injected into the solution with stirring for 2 h. Afterward, methanol solutions containing 2.5 g of Zn(NO₃)₂·6 H₂O (200 mL) and 3.0 g of 2-methylimidazole (200 mL) were added sequentially. The mixture was stirred for 24 h at 60 °C. After that, the precipitates, named PA@Fe-ZIF-8, were centrifuged, washed, and dried. The PA@Fe-ZIF-8 powder was milled and then pyrolyzed in the tube furnace at 1000 °C for 1 h under an argon atmosphere [20]. The NC and Fe-NC samples were prepared by essentially the same procedure as Fe-PNC, with the difference being the presence or absence of Fe(NO₃)₃·9H₂O and PA. The steps for the synthesis of the samples are shown in Fig. 1a.

2.3. Degradation experiments

The experiments were carried out in a glass beaker with 50 mL of aqueous BPA solution. The solution was reacted at 25 °C at a certain speed. And the batch tests were used to evaluate the PMS activation ability of various powders as catalysts. At specific time intervals throughout the process, 3 mL of the sample was filtered using a 0.22 µm filter and the results were measured using either a UV-Vis spectrophotometer or a liquid chromatograph. Each set of experiments were measured three times for averaging.

3. Results and discussion

3.1. Characterization of Fe-PNC and Fe-NC catalysts

The scanning electron microscope (SEM) was used to examine the structure and morphology of the Fe-NC and Fe-PNC materials. The Fe-NC and Fe-PNC catalysts both retain the dodecahedral morphology, and the morphology was not significantly damaged (Fig. 1b-c and S1). In addition, the aberration-corrected HAADF-STEM images show that some isolated bright spots can be observed in the sample (Fig. 1d). The EDS elemental mapping of the catalysts indicated that several elements were well dispersed in the range of 2–5 nm. In particular, the elements Fe and P appeared as single atoms and did not form nanoparticles or clusters (Fig. 1e and f) [21,22]. The above results indicate that atomically scattered Fe and P sites have been successfully loaded onto the carrier [23,24]. According to inductively coupled plasma emission spectroscopy (ICP), the Fe content in Fe-PNC is 1.42 wt%, which is slightly higher than the 1.36 wt% in Fe-NC. XPS analysis showed that the Fe(II) content of the sample increased after P-doping, indicating that Fe-PNC has a lower valence of chemistry than Fe-NC (Fig. 1g and Table S1). The N1s XPS spectra of Fe-NC and Fe-PNC catalysts showed a clear appearance of the several common peaks, including graphitic nitrogen, pyridine nitrogen, pyrrole nitrogen, and nitrogen oxides (Fig.S2) [25]. Some reports suggest that electron-rich pyridine N atoms on graphite

carriers can be used to coordinate with metal atoms. This may play a crucial role in stabilizing the single-atom Fe in the catalyst. In addition, the P2p XPS spectrum of the Fe-PNC catalyst showed three characteristic peaks from O-P, N-P, and C-P, which further confirmed the successful synthesis of P-atom modified Fe-N₄ catalyst (Fig. 1h).

The valence states of iron atoms in Fe-PNC were first analyzed using Fe K-edge XANES (Fig. 2a). The absorption edge of Fe-PNC is located between FeO and Fe₂O₃, which means that the valence state of Fe species in both samples is between the ranges of 2+ and 3+ [26,27]. Fe K-edge EXAFS was used to detect the geometrical configuration of the Fe-site in the locally coordinated Fe-PNC. In the Fourier transformed EXAFS R-space map (Fig. 2b), Fe-PNC shows a dominant peak at ~1.52 Å, which is ascribed to the coordination of monatomic Fe-N [28]. In contrast to the Fe foil, the Fe-Fe coordination peak at ~2.2 Å is absent in Fe-PNC, revealing that the Fe sites in Fe-PNC are a nature atomically dispersed [29]. The interatomic bond distance and coordination number of the central Fe in Fe-PNC were determined using EXAFS fit analysis. The best fit results for Fe-PNC were obtained by using two backscattering pathways for Fe-N and Fe-P (Fig. 2c). The coordination numbers of Fe-N and Fe-P for Fe-PNC were calculated to be 4.2 ± 0.3 and 2.2 ± 0.4 at the average distances of 1.99 ± 0.03 Å and 2.84 ± 0.02 Å, respectively (Table S2). Considering the coordination numbers, we propose a configuration of Fe-N₄-P₂, where N is located in the first coordination shell layer of the Fe center and P is located in the second coordination shell layer [30]. As shown in Fig. 2d-e, it can be clearly seen that for Fe-Se/NC, only one intensity maximum is detected at about 5.1 Å, which is attributed to the Fe-N bond, indicating that Fe is atomically dispersed in Fe-PNC without any aggregation of Fe nanoparticles or clusters (compared to Fe foils) [31]. The XRD patterns of Fe-PNC and Fe-NC catalysts showed similar graphite peaks compared to NC catalyst and no specific Fe crystal peaks were observed (Fig. 2f). These results further confirmed the absence of aggregated Fe nanoparticles in Fe-PNC and Fe-NC catalysts [32]. Hence, catalysts with atomic Fe-N₄ centers and neighboring type phosphorus atoms located in the second coordination shell layer have been successfully designed, which laid a solid foundation for the further application of electron-rich nonmetallic strategy modulated the valence and spin states of the metal center regulation of single atom catalyst.

3.2. Catalytic degradation properties of synthetic samples

The catalytic performance of the catalyst was evaluated comprehensively by the analysis of the BPA degradation efficiency and *k*_{obs}. As shown in Fig. 3a, it was concluded that the catalytic activity was in the order of Fe-PNC > Fe-NC > NC > pure Fe²⁺. Among in, PMS degraded only 10% of BPA in the absence of catalyst, and as a control measurement, the activation of PMS by pure Fe²⁺ and NC was also investigated, with degradation efficiencies of 51% and 56%, respectively, suggesting that PMS molecules cannot be efficiently activated to degrade bisphenol A in these two systems. To evaluate the effect of P-heteroatom-induced modulation of the electronic structure of the Fe center on regulating the activation activity of PMS, the performance of Fenton-like catalysts for BPA removal was evaluated. The original Fe-NC catalyst achieved 82% BPA degradation within 6 min. Notably, the electron-enriched Fe-N₄ site greatly facilitated the activation of PMS, and BPA was almost able to be completely degraded in the system using Fe-PNC as the catalyst. This result suggests that the P-induced Fe active site possesses a good performance in activating PMS to degrade BPA. To better compare the catalytic performance, the kinetics of BPA removal was then fitted by a pseudo primary reaction. The results showed that the degradation rate constants (*k*_{obs}) of Fe-PNC were 7.2 and 3.28 times higher than those of NC and Fe-NC, respectively. (Fig. 3b). The extent or rate constant of BPA degradation in the Fe-PNC/PMS system increases steadily with increasing PMS or catalyst dose (Fig.S3 and S4). Moreover, the degradation performance of BPA in the Fe-PNC/PMS system was superior to that of many advanced multiphase catalysts (Fig. 3c and Table S3)

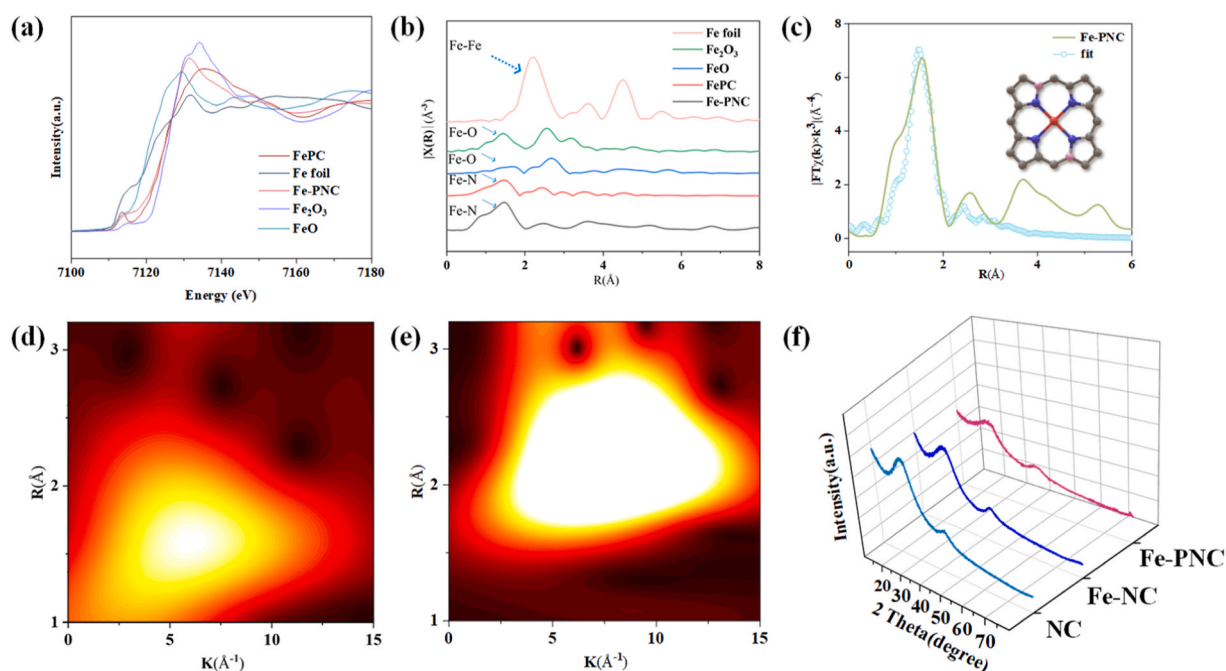


Fig. 2. (a) Normalized Fe K-edge XANES spectrum of Fe-PNC and the reference samples (Fe foil, FeO, FePC, and Fe₂O₃); (b) k^3 -weight FT-EXAFS fitting curves of Fe-PNC; (c) Fe K-edge FT-EXAFS spectra of Fe-PNC and reference samples (Fe foil, FeO, FePC and Fe₂O₃); WT-EXAFS plots of (d) Fe-PNC and (e) Fe foil; (f) XRD patterns of NC, Fe-NC and Fe-PNC.

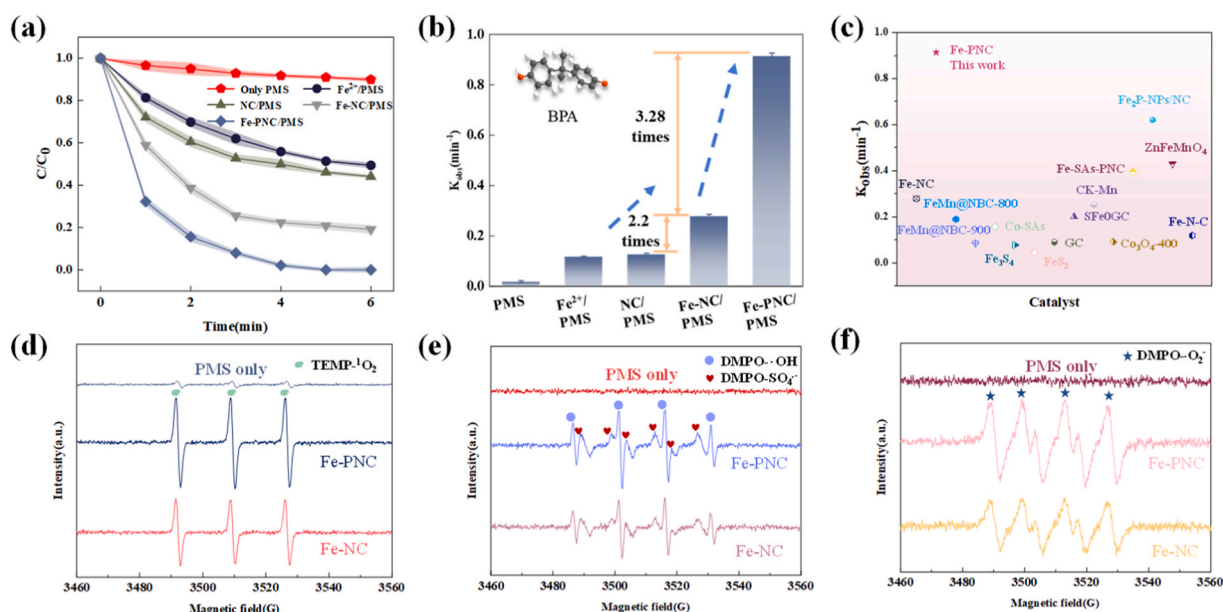


Fig. 3. (a) Degradation performance of BPA in different catalytic systems; (b) The k_{obs} values of BPA in different catalytic systems; (c) Comparison of the K_{obs} of BPA with catalysts reported in the literature; ESR spectra of (d) $^1\text{O}_2$; (e) $^{\bullet}\text{OH}$ and $\text{SO}_4^{\bullet-}$; and (f) $\text{O}_2^{\bullet-}$.

[33–39].

3.3. Identification of mechanisms in Fe-NC/PMS and Fe-PNC/PMS systems

The catalyst/PMS system was characterised using electron spin resonance (ESR) to identify reactive oxygen species in the Fe-PNC/PMS and Fe-NC/PMS systems [40]. As shown in Fig. 3d-f, for all catalysts, weak $\text{DMPO}\cdot\text{SO}_4^{\bullet-}$ signals, strong $\text{DMPO}\cdot^{\bullet}\text{OH}$ and $\text{DMPO}\cdot\text{O}_2^{\bullet-}$ signals, indicating the existence of these radicals in both Fe-PNC/PMS and Fe-NC/PMS systems. The ESR spectra showed enhanced $\text{TEMP}\cdot^1\text{O}_2$

signals observed in the catalyst/PMS system (Fig. 3d), suggesting the generation of $^1\text{O}_2$ in our reaction system [41]. In addition, the system was subjected to bursting experiments to further detect the effective type of ROS for degrading BPA. As shown in Fig. 4a and Fig.S5, MeOH was frequently acted as a bursting agent for hydroxyl and sulfate radical. The degradation of BPA by both catalysts was also not significantly reduced when the dose ratio of MeOH: PMS was adjusted to 500:1. The similar results were obtained using TBA as a free radical bursting agent; when the ratio of TBA: PMS was increased from 100:1–500:1, the bursting influence of TBA on the removal of BPA was minimal. Similarly, the use of P-BQ as a bursting agent has little effect on the degradation of

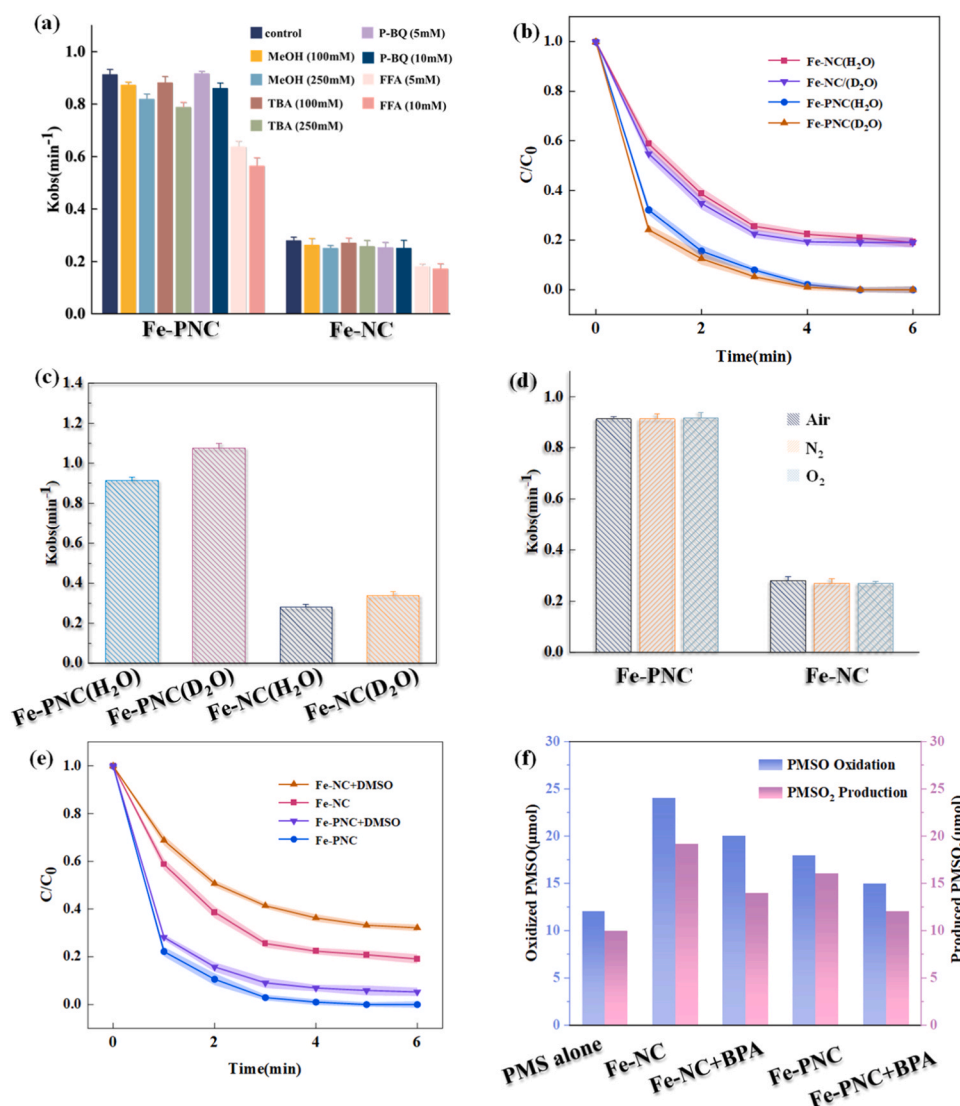


Fig. 4. (a) The k_{obs} values of BPA oxidation in Fe-PNC/PMS and Fe-NC/PMS systems with different scavengers; (b) The k_{obs} of BPA oxidation in H₂O and D₂O solutions; (c) BPA oxidation in Fe-PNC/PMS and Fe-NC/PMS systems by replacement of H₂O with D₂O; (d) Degradation rate of BPA by Fe-PNC and Fe-NC activated PMS under different atmospheres; (e) The inhibition of DMSO on BPA degradation by Fe-NC/PMS and Fe-PNC/PMS system. (f) The oxidation of PMSO and the generation of PMSO₂ in PMS systems activated by different catalysts ([PMS] = 0.5 mM, [catalyst] = 0.1 g L⁻¹, [DMSO] = 10 mM, [PMSO] = 50 μM).

BPA. The results suggest that the $SO_4^{\bullet-}$, $\bullet OH$, and $O_2^{\bullet-}$ radicals are not the leading species in both systems and may be masked by other pathways [42]. Considering that 1O_2 can be formed when carbon catalysts are involved in PMS activation, FFA was used as a 1O_2 probe. The degradation of BPA was hindered by both Fe-NC/PMS and Fe-PNC/PMS systems when the ratio of FFA to PMS was 20:1, and the degradation time was prolonged from 6 min to 10 min (Fig. S5). The role of 1O_2 was further determined using D₂O as a solvent, because the lifetime of 1O_2 was more than 10 times longer in D₂O than in H₂O. The results in Fig. 4b and c show that the degradation rate is slightly increased, but the degree of degradation is almost constant by the replacement of H₂O with D₂O. These burst results suggest that the negligible contribution of 1O_2 to BPA degradation and that there are other pathways exerted contribution to BPA degradation. The atmosphere (N₂, O₂, or air) did not affect the degradation rate of BPA, indicating that the O species of 1O_2 was not from dissolved oxygen (Fig. 4d and Fig. S6). Meanwhile, the degradation degree of BPA in the existence of p-BQ was almost unchanged, suggesting that $O_2^{\bullet-}$ is not the cause of 1O_2 production (Fig. 4a). The above results indicate that Fe-NC and Fe-PNC can directly activate PMS to produce 1O_2 , but do not take a key role to degrade BPA.

In transition metal-based PMS-activated systems, it is expected that the high-valent metal species contribute to the organic degradation efficiency [43]. Dimethyl sulfoxide (DMSO) was used as a probe to quench the production of high-valent iron species. In the Fe-NC/PMS system, the

degradation degree of BPA was reduced by 14% by the excessive addition of DMSO (DMSO/PMS ratio of 20:1) (Fig. 4e), whereas in the Fe-PNC/PMS system, the degradation degree of BPA was reduced by only 4.7%. Furthermore, the consumption of PMSO and the generation of PMSO₂ in the system were evaluated by comparing it with a single PMS system, and the oxidative conversion of PMSO to PMSO₂ was further used to quantify the involvement of high-valent metal oxygen species. As shown in Fig. 4f, the oxidation of PMSO and the production of PMSO₂ were detected in both Fe-NC/PMS and Fe-PNC/PMS systems. Approximately 10% of PMSO was consumed in the PMS system only, this result may be due to the fact that PMS can also generate PMSO₂ by reacting with PMSO, however, both the consumption of PMSO and the yield of PMSO₂ were more in the Fe-NC/PMS system than in the Fe-PNC/PMS system. The addition of BPA inhibits the reaction, indicating that the formed high-valent metal oxides exhibit some reactivity towards BPA [44]. According to different burst tests on BPA degradation, high-valent iron plays a weak role in BPA degradation, and the degradation of BPA in the Fe-PNC and Fe-NC catalytic systems should take place mainly through free radical and other non-radical pathways.

3.4. Study of electron transfer paths in several catalyst systems

If the main cause of contaminant degradation is non-radicals, the premixing of PMS and catalyst has little effect on contaminant

degradation [32]. This is evident from the negligible inhibition of BPA degradation when Fe-NC and Fe-PNC were premixed with PMS for different durations (1, 3, and 5 mins) (Fig. 5a and Fig.S7). These results suggest that the electron flow between the catalyst and the contaminant primarily occurs through non-radical pathways during BPA degradation. Interestingly, a steady decrease in the observed rate constant (k_{obs}) of BPA was observed with increasing premixing times from 1 min to 5 min. This finding further supports the notion that although radicals do contribute to BPA degradation in both catalytic systems, non-radical pathways play a dominant role.

The open circuit potential can be used to determine the electron transfer pathway in the catalytic system [45]. Significantly different potential changes were observed in different catalyst/PMS/BPA systems (Fig. 5b). The complex potentials of several catalyst/PMS systems were found to be approximately 0.99 V for Fe-PNC/PMS, 0.90 V for Fe-NC/PMS, and only 0.623 V for NC/PMS. These results indicate that Fe-PNC can form stronger substitutable intermediates (Fe-PNC/PMS*) with PMS, leading to an elevated oxidation potential of Fe-N₄P₂ and initiating the electron transfer pathway more effectively than Fe-NC/PMS*. In addition, the Fe-PNC/PMS* complex will act as a mediator to extract electrons from the adsorbed pollutants, ultimately lowering the potential of the Fe-N₄P₂-C catalyst and releasing $\cdot\text{OH}$ and SO_4^{2-} ions. Moreover, the addition of BPA at 3620 s showed different degrees of potential decrease in Fe-PNC/PMS* and Fe-NC/PMS* compared to NC/PMS*, with a higher degree of decrease in Fe-PNC/PMS*. In contrast, the potential fluctuations were minimised in the NC/PMS system. The above findings suggest that an intense electron transfer occurs between BPA and the Fe-PNC catalyst within the Fe-PNC/PMS system. Overall, these results provide evidence for the use of electron transfer pathways involved in catalytic oxidation using Fe-PNC and PMS. The strong electron transfer process observed in the Fe-PNC/PMS system highlights its effectiveness in facilitating pollutant degradation through efficient electron extraction from adsorbed pollutants. In addition, the EIS Nyquist plots of Fe-PNC were much smaller than those of the other catalysts, suggesting a lower charge transfer resistance and better electron transfer process compared to the other catalysts (Fig. 5c).

The reaction processes occurring in the Fe-PNC/PMS system were

investigated using in situ Raman spectroscopy tests. It can be seen that the peaks located at 987, 887, and 1067 cm^{-1} were assigned to SO_4^{2-} , O-O and SO_3 , respectively (Fig. 5d). Compared to the pure PMS solution, the addition of Fe-PNC resulted in a new peak at 835 cm^{-1} corresponding to the extended bending vibration of the peroxide O-O bond in the Fe-PNC/PMS* complex [46]. The characteristic peak of the Fe-PNC/PMS* complex diminished after BPA addition and the I_{1067}/I_{987} ratio decreased, implying a faster PMS consumption due to the fast HSO_5^- -to- SO_4^{2-} transformation via radical pathway. Surprisingly, the peak of Fe-PNC/PMS* complex disappeared 5 min into the Fe-PNC/PMS system caused by the intense electron transfer process between the BPA and Fe-PNC/PMS* complexes due to the accelerated decomposition of PMS. When BPA was introduced for 20 min, only the characteristic peak of SO_4^{2-} was retained at 987 cm^{-1} , and several other characteristic peaks disappeared completely.

To further demonstrate this mechanism, we further analyzed the electron transfer between BPA and Fe-PNC/PMS using an electron-coupled oxidation system (GOS) by separating PMS and BPA into two electrolytic cells connected by placing PMS and BPA in two electrolytic cells, connecting them with a salt bridge and an ammeter, and applying catalysts to the working electrodes, to observe the current changes and pollutant degradation during the reaction. In this system, BPA can only be oxidized by direct electron transfer (Fig. 5e). As shown in Fig. 5f, a large increase in current was recorded when the graphite electrode was coated with the catalyst, and the current values of Fe-PNC, Fe-NC, and NC rapidly reached the maximum value throughout the reaction and then gradually decreased with the maximum currents of 65 μA , 48 μA , and 35 μA , respectively. Moreover, more BPA could be oxidized by the Fe-PNC catalyst in GOS (Fig. S8). This result indicates that BPA can be oxidized by direct electron transfer. Such results further confirm that Fe-PNC can provoke more electron transfer than Fe-NC and NC. Moreover, the Fe-PNC catalyst in GOS can oxidize and toward more BPA degradation.

3.5. DFT calculations and analysis

In depth elucidation of the effect of P doping on Fe single-atom catalysts using DFT calculations. First, the energy barriers for the

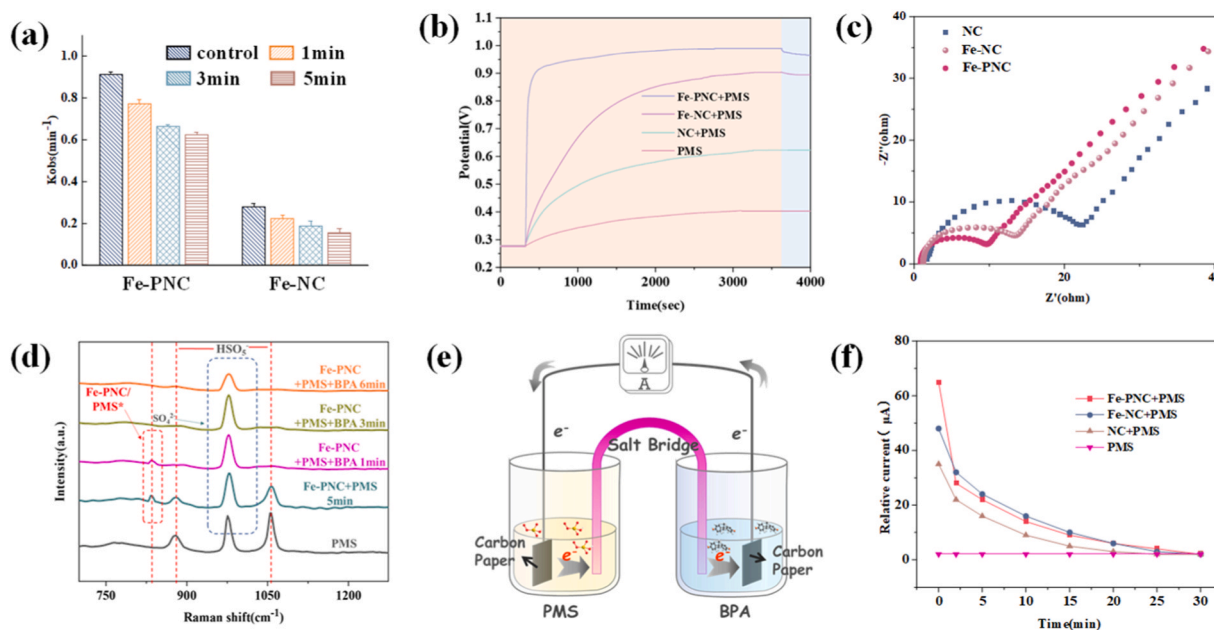
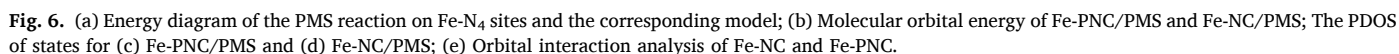


Fig. 5. (a) The K_{obs} of Fe-PNC and Fe-NC catalysts premixed with PMS systems; (b) Open-potential in different systems; (c) EIS Nyquist plots of NC, Fe-NC and Fe-PNC catalysts; (d) In situ Raman spectroscopy and BPA degradation catalyzed by Fe-PNC that precontacted with PMS; (e) A scheme of GOS system; (f) Current changes in GOS systems with different catalyst coatings (Fe-PNC, Fe-NC and NC).

thermodynamic processes of $\text{SO}_4^{\bullet-}$ and $\bullet\text{OH}$ generation are favorable in the Fe-PNC/PMS system. Second, the charge transfer (Q_e) from the Fe site to the O site of PMS was calculated, and the Q_e of Fe-PNC was elevated after doping P around the Fe atom (Table S4). The higher Q_e values indicate that the PMS molecule gains electrons more easily in the activation reaction, leading to a greater extension of the O-O bond of



PMS, which further indicates PMS adsorbed with the Fe-N₄-P₂ site was more energy favorable as compared with that adsorbed with the Fe-N₄ site. Meanwhile, the front-line molecular orbital theory suggests the importance of the HOMO and LUMO. The energy difference between HOMO and LUMO (E_{L-H}) was often used to characterize the electronic structural properties of the materials, and a smaller E_{L-H} usually leads to higher chemical reactivity. The E_{L-H} of PMS and Fe-PNC are 8.12 and 0.84 eV, respectively. The E_{L-H} decreased to 0.75 eV after PMS adsorption on the Fe centre site of the catalyst, suggesting that the reactivity of PMS was enhanced after adsorption on the Fe center of the complex (Fig. 6b). For Fe-NC, the E_{L-H} of PMS dropped to 1.12 eV after adsorption on the surface. And the E_{L-H} of Fe-PNC/PMS and Fe-NC/PMS were lower than that of PMS alone, indicating that both of them can activate PMS to produce electron transfer. But, in comparison to Fe-NC/PMS, it is more beneficial for the formation of the oxidation reaction to progress due to lower the energy gap energy being based on the Fe-PNC/PMS. Thus, DFT calculations indicate that the introduction of P elements in the second coordination shell layer can effectively improve the catalyst reactivity by lowering the energy barrier for the reaction of Fe active sites with PMS and enhancing the charge transfer between Fe sites and PMS. Indeed, the catalytic activity is strongly correlated with the internal structure of the Fe active site. By comparing the changes in the electronic structure of different catalysts, it is possible to gain more insight into the effect of P doping on BPA degradation.

According to Fig.S9, the introduced element P effectively increases the electron density of Fe atoms in the catalyst. This is consistent with the results of valence analysis by XPS. In addition, the density of states analysis (Figs. 6c-d and S10) showed that the PDOS of Fe-PNC was shifted in the positive direction with a higher d-band center (−3.343 eV) compared to Fe-NC (−3.890 eV), suggesting that the presence of P increased the d-band center and 3d energy band energy of the Fe cation, thereby facilitating electron transfer and enhancing the reactivity of the catalyst with PMS. Moreover, in Fe-PNC, the PDOS of Fe shifts in the high-energy direction and the d-band center rises to −2.684 eV after adsorption, and the adsorption energies (E_{ads}) of PMS show that the localized electrons and the delocalized charge accumulate along the metal center, implying a strong binding for PMS molecule between Fe-N₄P₂ sites and adsorbed oxygen species in Fe-PNC become stronger in comparison with the Fe-NC. Furthermore, the shift of Fe-PDOS to the high-energy direction is usually accompanied by a change of the Fe-3d electron spin state, thus leading to a shift of the 3d electronic spin state of Fe atom from low to high spin.

To obtain direct experimental proof, the effective magnetic moment (μ_{eff}) was calculated from the χ^{-1} -T curve (Fig.S11–12) [47]. Compared with Fe-NC, the μ_{eff} value of Fe-PNC is significantly increased, which indicates that the Fe-PNC catalyst has a higher spin state than Fe-NC. μ_{eff} value is positively correlated with the K value of the catalyst, indicating that the spin state plays a key role in the high reactivity of the catalyst. Due to the transfer of electrons from organic molecules to metal-oxygen π^* orbitals at low locations consistent with the spin state crossover, the high-spin Fe-PNC can achieve a relatively low oxidation energy barrier path, which is consistent with the above DFT analysis and open-circuit potential results.

Meanwhile, the spin number and the number of unpaired electrons of the Fe-PNC and Fe-NC catalysts were estimated based on the theoretical equations of μ_{eff} (Table S5). Since the single-atom models of Fe-NC and Fe-PNC can be analysed by ligand field theory. It can be roughly inferred that Fe-NC loads the LS state while Fe-PNC maintains a high spin state. That is, the doping of P element not only increases the electron density of Fe-PNC, but also increases the number of unpaired electrons. The introduction of P element induces the localized delocalization of Fe 3d electrons, indicating that the effect of P may promote the transfer of 3d electrons from Fe to O 2p orbitals. For the activation of PMS, the action of P increases the energy of Fe 3d electrons, which makes it easier to transfer electrons from Fe to the O2p orbitals of PMS. The increase of unpaired electrons induced by P doping is a key factor to enhance the

activation of PMS. In summary, the mechanism of P doping to enhance the catalyst reactivity with PMS for the degradation of BPA was proposed (Fig. 6a and b). By introducing P element into the Fe active site, the electron density of the Fe site is increased, while the splitting energy of the coordination field is reduced, thus keeping the Fe site in Fe-PNC in a high spin state at all times. To further understand the reason for the enhanced reactivity of Fe-PNC, we determined the magnetic properties of Fe-PNC and the spin state of the Fe sites. These results were further confirmed by the formation of Fe-N₄P₂ sites on Fe-PNC were observed, showing the existence of Fe-P-N coordination by P-anchored Fe single-atom catalysts.

Ligand field theory suggests that when a metal center is coordinated with a weak-field ligand, it is usually in a high-spin state, versa vise. As shown in Fig. 6e, the complex formed by the Fe center and the PNC ligand forms high-energy e_g^* orbitals and low-energy t_{2g} orbitals, which allows for easier transfer of electrons from the ligand to the metal center, resulting in the Fe center site at high spin state. However, the complexes formed by Fe with NC ligands produce low-energy e_g^* orbitals and high-energy t_{2g}^* orbitals, leading to a reduction in the transfer of electrons from the NC ligand to the Fe center, which inhibits the electron-giving properties of the metal. Considering the presence of high spin-dominated metal species in Fe-PNC, it can be regarded as a coordination compound formed by Fe with weak field ligands, while Fe-NC is regarded as a coordination compound formed by Fe with strong field ligands. It can be seen that the interaction of the ligand's orbitals with the 3d orbitals of Fe will result in the formation of new molecular orbitals, including a low-energy bonding orbital (t_{2g}) and a high-energy antibonding orbital (t_{2g}^*). dxy in Fe^{II} and dyz, dxz in the ligand will occupy the antibonding orbitals (t_{2g}^*), while dz^2 and dx^2y^2 will occupy the e_g^* orbitals.

The high spin nature of the complexes facilitates the transition of the "d-d" ligand field from t_{2g} to e_g^* . Notably, the gap between e_g^* and t_{2g}^* in Fe-PNC complexes is 2.74 eV, which is significantly smaller than that of Fe-NC complexes (3.11 eV), indicating that Fe-PNC complexes have a stronger tendency to give electrons. Considering that the t_{2g} orbital is occupied by off-domain electrons, the metal center in Fe-PNC will act as a strong electron acceptor, which is conducive to the maintenance of a high spin state in the central site of Fe, thus improving the activity and stability of the catalytic reaction. Thus, it is possible to keep the Fe center in a high spin state, which facilitates the continuous oxidation of pollutants.

3.6. Degradation performance in Fe-PNC/PMS system

It can be observed in Fig. 7a and Fig.S13 that all anions (Cl^- , F^- , HCO_3^- , NO_3^- , CO_3^{2-} , $H_2PO_4^-$ and PO_4^{3-}), cations (Na^+ , Mg^{2+} , K^+ , and Ca^{2+}) and NOM did not inhibit the degradation of BPA. It suggests that the degradation of BPA degradation by Fe-PNC is less affected by common interfering substances in water [48]. In addition, Fe-PNC effectively activated PMS to degrade BPA in the pH range of 3–11 (Fig. 7b, Fig.S14 and Table S6), indicating that the Fe-PNC catalyst was highly tolerant to the pH of the solution. Nevertheless, the degradation rate of BPA showed slight differences at different pH, which may be due to the effect of pH on the zeta potential of Fe-PNC and the form of BPA present (Fig.S15) [4]. More importantly, the degradation rate of Fe-PNC for BPA in natural water (tap water, Kongmu lake water, sludge water, and farming wastewater) and deionized water decreased but both reached more than 50%, indicating that it has good prospects for practical water purification applications (Fig. 7c and Fig.S16). As shown in Fig.S17, the cycling experiments demonstrated that Fe-PNC was able to degrade BPA stably during the activation of PMS. In summary, the Fe-PNC activated PMS system has excellent performance and good potential for application.

Powder catalyst activation of PMS is a water pollution control method that is difficult to recover and prone to secondary pollution (Fig. 7d). SEM images confirmed that the Fe-PNC catalyst was well dispersed on the carbon felt (Fig. 7e) [49]. The dynamic adsorption and

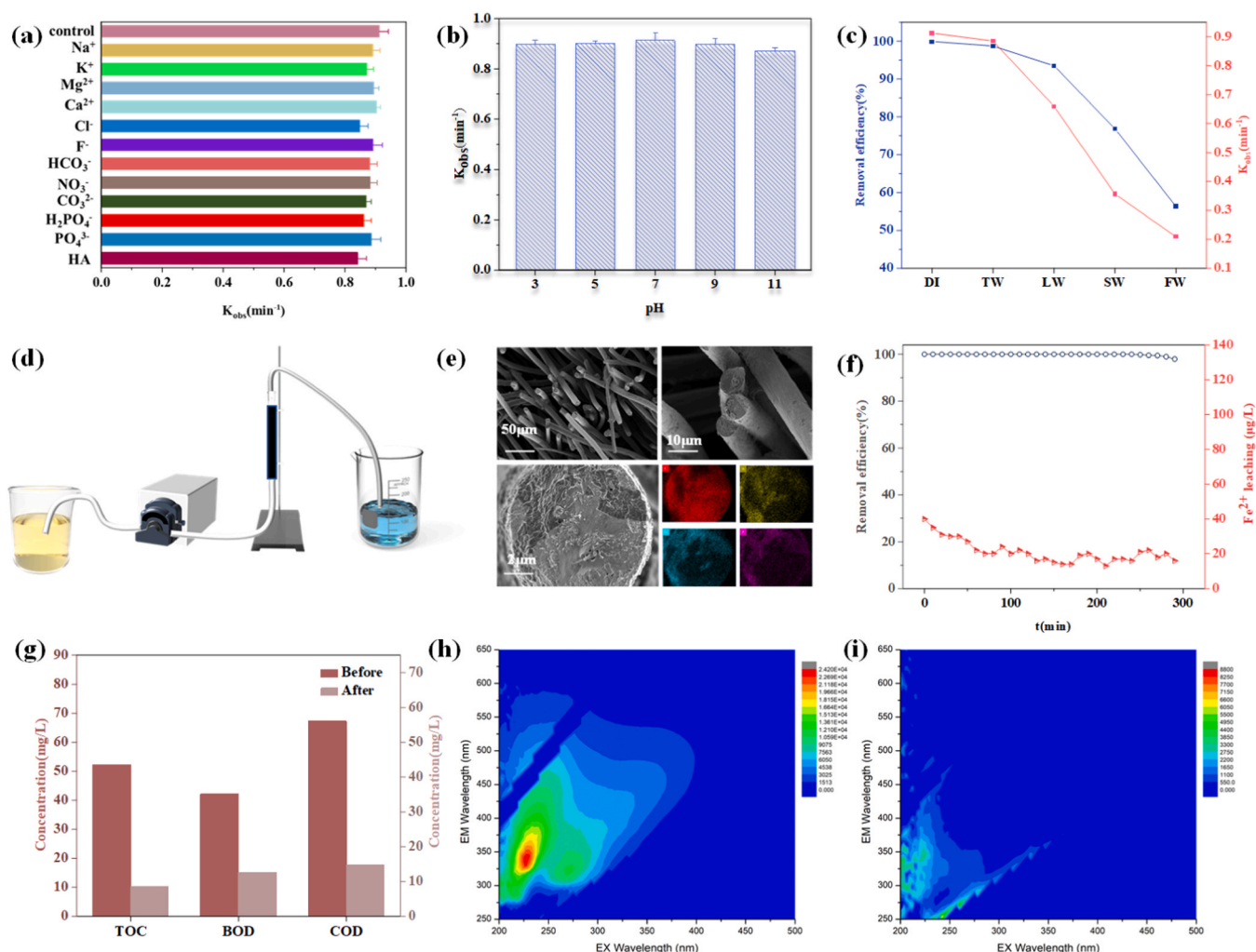


Fig. 7. (a) Degradation rate of BPA in Fe-PNC/PMS system in the existence of different interfering substances; (b) Removal rate of BPA at different initial pH; (c) Degradation rate and k_{obs} of Fe-PNC-activated PMS system for BPA in different natural waters; (d) catalytic filtration device; (e) scanning electron microscopy and EDS mapping at its different scales; (f) catalytic system for BPA degradation; (g) removal of several indicators in the water by the catalytic filtration device; 3D fluorescence spectra (h) before and (i) after the reaction.

catalytic processes demonstrated that the Fe-PNC/PMS system displayed excellent purification performance with only trace Fe leaching within 290 min (Fig. 7f). This further suggests that the Fe-PNC/PMS system has some potential applications in water pollution control.

Given its excellent reaction performance, we evaluated the utility of the Fe-PNC/PMS catalytic reactor in degrading BPA in real domestic wastewater samples and in treating real industrial wastewater samples by PMS activation. The actual wastewater samples were collected from biologically treated wastewater from an industrial park in Jiangxi Province. And the composition of the water samples are shown in Table S6. Fig. 7g shows the good removal of BPA by the catalytic system in a real wastewater sample, where the Fe-PNC activated PMS effectively destroyed the organic matter in the 3DEEM fluorescence spectra of this real wastewater sample (Fig. 7h-i). This demonstrates the excellent performance and stability of Fe-PNC catalysts for water pollution control.

3.7. BPA degradation pathways and intermediates

Intermediates and potential reaction paths of BPA in the Fe-PNC/PMS system were predicted by HOMO and LUMO orbital analyses, Fukui functions and LC-MS characterization. Fig. 8a shows the molecular structure and the HOMO and LUMO orbital isosurfaces,

respectively, that can be used to describe the electron-donating and electron-accepting capacity of the BPA molecule during the oxidation process. The HOMO of BPA is mainly focused on the O, C11, C12, and C16 atoms and the two benzene rings, which are prone to attack by electrophilic reagents, whereas the LUMO is focused on the symmetric benzene ring, which is susceptible to attack by nucleophilic reagents.

Fukui indices were also employed to point out vulnerable sites of BPA molecules from the electronic structure perspective and the calculated values are shown in Fig. 8b [50]. Combining the above results analysis, possible pathways for BPA oxidation were proposed (Fig. 8c and Fig.S18). Due to the high f value of the C3(C20) site, the consecutive bonds of C3(C20) and C11 are susceptible to electrophilic attack, resulting in the cleavage of the C-C bond to form P1 and P2, and further oxidation to P3, P7, and P8. Moreover, the C6(C27) site of the BPA molecule is also susceptible to electrophilic attack and undergoes dehydroxylation to form P4, which then generates P7, and P8. Due to the high f -value and highest f^+ and f^0 values, the C5(C25) site of the BPA molecule is most susceptible to attack and undergoes hydroxylation to form P5, which then undergoes hydroxylation. Since the C5(C25) site of the bisphenol A molecule has a high f value and the highest f^+ and f^0 values, it is most susceptible to attack and hydroxylation reaction to produce P5, which is then converted to P6 by dehydroxylation reaction, and finally produces P7 and P8.

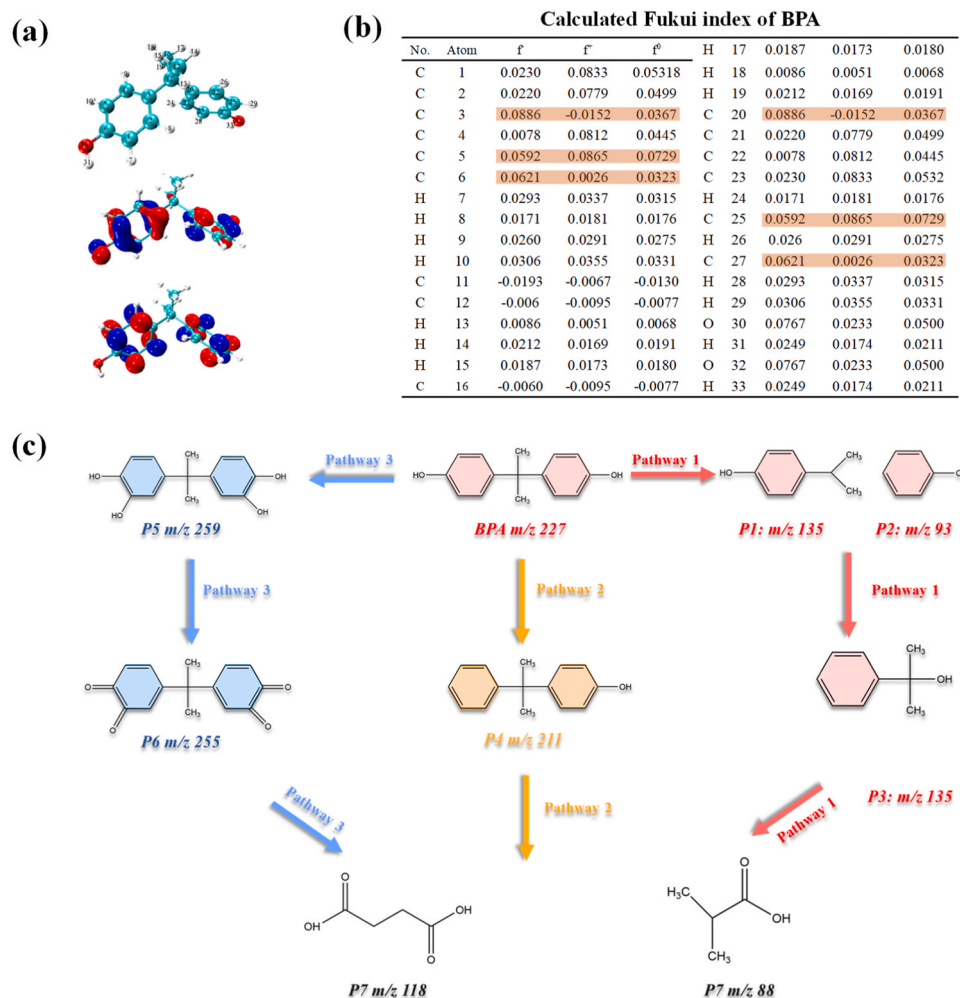


Fig. 8. (a) Chemical structure molecule, HOMO and LUMO orbitals of BPA; (b) Fukui values of all atoms in the BPA; (c) Intermediates and potential transformation pathways of BPA in the Fe-PNC/PMS system.

4. Conclusions

This study shows that phosphorus doping in the second shell layer can significantly enhance the reactivity of single Fe atom catalysts for PMS. The underlying mechanism was elucidated based on experimental studies and DFT calculations. The results showed that P doping of the second shell layer effectively modulated the electron density and structure of Fe atoms, which further significantly improved the catalytic activity of PMS. As a result of P doping, the energy enhancement of the Fe 3d orbital electrons induced the production of more unpaired electrons, which led to the transition of the catalyst from the original low-spin state to the high-spin state. This led to a better combination of the Fe3d orbitals with the O2p orbitals of PMS, which resulted in the transfer of more electrons from the Fe site to PMS and accelerated the decomposition of PMS, leading to the degradation of BPA. In addition, P doping reduced the splitting field energy as well as the energy gap of the catalyst, which prompted the fast and efficient transfer of electrons from the BPA to the Fe sites and kept Fe in a higher spin state, thus achieving the sustained degradation of BPA. Finally, the doping of P in the second shell layer modulates the electron density and structure of the Fe active center at the atomic level, which provides a more comprehensive understanding of the process of PMS activation at the atomic level, and can provide insights into the development of highly efficient metal single-atom catalysts.

CRediT authorship contribution statement

Yandong Chai: Investigation, Methodology, Writing – original draft, Visualization. **Hongling Dai:** Resources, Writing – review & editing, Supervision. **Xiaoguang Duan:** Resources, Writing – review & editing. **Zhiqiang Sun:** Conceptualization, Writing – review & editing, Supervision. **Fengping Hu:** Conceptualization, Writing – review & editing, Supervision. **Jin Qian:** Conceptualization, Writing – review & editing, Supervision. **Xiaoming Peng:** Conceptualization, Methodology, Writing – review & editing.

Declaration of Competing Interest

The authors declare that they have no known competing financial interests or personal relationships that could have appeared to influence the work reported in this paper.

Data Availability

Data will be made available on request. No data was used for the research described in the article.

Acknowledgements

This work was supported by the Natural Science Foundation of China (No. 52160001), Outstanding Youth Science Foundation of Jiangxi

Province (NO.20224ACB213009), the Natural Science Foundation of Jiangxi Province (No. 20212ACB204003), Science and Technology Project of Water Resources Department of Jiangxi Province (NO.7, 202223YBKT44) and State Key Laboratory of Pollution Control and Resource Reuse Foundation (No. PCRRF21028).

Appendix A. Supporting information

Supplementary data associated with this article can be found in the online version at [doi:10.1016/j.apcatb.2023.123289](https://doi.org/10.1016/j.apcatb.2023.123289).

References

- [1] Y. Zhao, S. Chen, H. Qie, S. Zhu, C. Zhang, X. Li, W. Wang, J. Ma, Z. Sun, Selective activation of peroxymonosulfate govern by B-site metal in delafossite for efficient pollutants degradation: pivotal role of d orbital electronic configuration, *Water Res.* 236 (2023), 119957, <https://doi.org/10.1016/j.watres.2023.119957>.
- [2] S. Li, M. Zhou, H. Wu, G. Song, J. Jing, N. Meng, W. Wang, High-efficiency degradation of carbamazepine by the synergistic electro-activation and bimetal (FeCo@NC) catalytic-activation of peroxymonosulfate, *Appl. Catal. -B: Environ.* 338 (2023), 123064, <https://doi.org/10.1016/j.apcatb.2023.123064>.
- [3] Y. Liu, H. Zhou, C. Jin, C. Tang, W. Zhang, G. Liu, L. Zhu, F. Chu, Z. Kong, Bio-porphyrin supported single-atom iron catalyst boosting peroxymonosulfate activation for pollutants degradation: a singlet oxygen-dominated nonradical pathway, *Appl. Catal. -B: Environ.* 338 (2023), 123061, <https://doi.org/10.1016/j.apcatb.2023.123061>.
- [4] Y. Chai, H. Dai, P. Zhan, Z. Liu, Z. Huang, C. Tan, F. Hu, X. Xu, X. Peng, Selective degradation of organic micropollutants by activation of peroxymonosulfate by Se@NC: Role of Se doping and nonradical pathway mechanism, *J. Hazard. Mater.* 452 (2023), 131202, <https://doi.org/10.1016/j.jhazmat.2023.131202>.
- [5] W. Song, C. Xiao, J. Ding, Z. Huang, X. Yang, T. Zhang, D. Mitlin, W. Hu, Review of Carbon Support Coordination Environments for Single Metal Atom Electrocatalysts (SACS), *Adv. Mater.* n/a (2023), 2301477, <https://doi.org/10.1002/adma.202301477>.
- [6] K. He, L. Hao, Youji Li, Peng Zhang, Jizhou Jiang, Xin Li, Advances in Nanostructured Silicon Carbide Photocatalysts, 2201021-, *Acta Phys. -Chim. Sin.* 38 (2022), <https://doi.org/10.3866/pku.WHxb202201021>.
- [7] Kaining Li, Xiaoyu Ou, Ruina Li, Qin Li, Jiajie Fan, Kangle Lv, Strategies for the Fabrication of 2D Carbon Nitride Nanosheets, 2008010-, *Acta Phys. -Chim. Sin.* 37 (2021), <https://doi.org/10.3866/pku.WHxb202008010>.
- [8] Y. Shang, X. Xu, B. Gao, S. Wang, X. Duan, Single-atom catalysis in advanced oxidation processes for environmental remediation, *Chem. Soc. Rev.* 50 (2021) 5281–5322, <https://doi.org/10.1039/D0CS01032D>.
- [9] Z. Mukadam, S. Liu, A. Pedersen, J. Barrio, S. Fearn, S.C. Sarma, M.-M. Titirici, S. B. Scott, I.E.L. Stephens, K. Chan, S. Mezzavilla, Furfural electrocatalysis using single-atom molecular catalysts, *Energ. Environ. Sci.* (2023), <https://doi.org/10.1039/D3EE000551H>.
- [10] J. Miao, J. Song, J. Lang, Y. Zhu, J. Dai, Y. Wei, M. Long, Z. Shao, B. Zhou, P.J. J. Alvarez, L. Zhang, Single-Atom MnN5 Catalytic Sites Enable Efficient Peroxymonosulfate Activation by Forming Highly Reactive Mn(IV)-Oxo Species, *Environ. Sci. Technol.* 57 (2023) 4266–4275, <https://doi.org/10.1021/acs.est.2c08836>.
- [11] L. Wang, H. Chen, Y. Wang, X. Liu, C. Li, J. He, T. Yao, Recent advances in regulating the local environment of M-N4 structure for tailored chemical reactions, *Nano Res.* (2023), <https://doi.org/10.1007/s12274-023-5510-8>.
- [12] Y. Gao, B. Liu, D. Wang, Microenvironment Engineering of Single/Dual-atom Catalysts for Electrocatalytic Application, *Adv. Mater.* n/a (2023), 2209654, <https://doi.org/10.1002/adma.202209654>.
- [13] V. Giulimondi, S. Mitchell, J. Pérez-Ramírez, Challenges and Opportunities in Engineering the Electronic Structure of Single-Atom Catalysts, *ACS Catal.* 13 (2023) 2981–2997, <https://doi.org/10.1021/acscatal.2c05992>.
- [14] K. Liu, J. Fu, Y. Lin, T. Luo, G. Ni, H. Li, Z. Lin, M. Liu, Insights into the activity of single-atom Fe-N-C catalysts for oxygen reduction reaction, *Nat. Commun.* 13 (2022), 2075, <https://doi.org/10.1038/s41467-022-29797-1>.
- [15] Z. Han, Y. Zhu, X. Yao, H. Peng, C. Du, J. Tian, L. Yang, X. Ma, J. Hou, C. Cao, Boosting oxygen reduction of single atomic iron sites by charge redistribution, *Appl. Catal. -B: Environ.* 337 (2023), 122961, <https://doi.org/10.1016/j.apcatb.2023.122961>.
- [16] Z. Qi, Y. Zhou, R. Guan, Y. Fu, J.-B. Baek, Tuning the Coordination Environment of Carbon-Based Single-Atom Catalysts via Doping with Multiple Heteroatoms and Their Applications in Electrocatalysis, *Adv. Mater.* n/a (2023), 2210575, <https://doi.org/10.1002/adma.202210575>.
- [17] L. Yin, S. Zhang, M. Sun, S. Wang, B. Huang, Y. Du, Heteroatom-Driven Coordination Fields Altering Single Cerium Atom Sites for Efficient Oxygen Reduction Reaction, *Adv. Mater.* n/a (2023), 2302485, <https://doi.org/10.1002/adma.202302485>.
- [18] Y. Zhang, X. Chen, C. Liang, L. Yin, Y. Yang, Reconstructing the coordination environment of single atomic Fe-catalysts for boosting the Fenton-like degradation activities, *Appl. Catal. -B: Environ.* 315 (2022), 121536, <https://doi.org/10.1016/j.apcatb.2022.121536>.
- [19] X. Zhou, M.-K. Ke, G.-X. Huang, C. Chen, W. Chen, K. Liang, Y. Qu, J. Yang, Y. Wang, F. Li, H.-Q. Yu, Y. Wu, Identification of Fenton-like active Cu sites by heteroatom modulation of electronic density, *Proc. Natl. Acad. Sci.* 119 (2022), e2119492119, <https://doi.org/10.1073/pnas.2119492119>.
- [20] Y. Zhou, R. Lu, X. Tao, Z. Qiu, G. Chen, J. Yang, Y. Zhao, X. Feng, K. Müllen, Boosting Oxygen Electrocatalytic Activity of Fe-N-C Catalysts by Phosphorus Incorporation, *J. Am. Chem. Soc.* 145 (2023) 3647–3655, <https://doi.org/10.1021/jacs.2c12933>.
- [21] T. Wu, S. Zhu, Y. Xie, Q. Ma, C. Lu, NaNO₃ assisted gelatin-derived multi-level porous carbon aerogel loaded Fe single-atom for high efficient oxygen reduction reaction, *Appl. Catal. -B: Environ.* 331 (2023), 122685, <https://doi.org/10.1016/j.apcatb.2023.122685>.
- [22] Rongchen Shen, Qing Chen, Qiaoling Zheng, Peng Zhang, Xin Li, P-Doped g-C₃N₄ Nanosheets with Highly Dispersed Co_{0.2}Ni_{1.6}Fe_{0.2}P Cocatalyst for Efficient Photocatalytic Hydrogen Evolution, *Acta Phys. -Chim. Sin.* 38 (2022) 2110014, <https://doi.org/10.3866/pku.WHxb202110014>.
- [23] K. Yin, L. Peng, D. Chen, S. Liu, Y. Zhang, B. Gao, K. Fu, Y. Shang, X. Xu, High-loading of well dispersed single-atom catalysts derived from Fe-rich marine algae for boosting Fenton-like reaction: Role identification of iron center and catalytic mechanisms, *Appl. Catal. -B: Environ.* 336 (2023), 122951, <https://doi.org/10.1016/j.apcatb.2023.122951>.
- [24] J. Cui, L. Li, Y. Wu, J. Gao, K. Wang, C. Diao, C. Hu, Y. Zhao, Robust Fe-N4 center with optimized metal-support interaction for efficient pollutant degradation by Fenton-like reaction, *Appl. Catal. -B: Environ.* 331 (2023), 122706, <https://doi.org/10.1016/j.apcatb.2023.122706>.
- [25] Y. Gao, Y. Zhu, T. Li, Z. Chen, Q. Jiang, Z. Zhao, X. Liang, C. Hu, Unraveling the High-Activity Origin of Single-Atom Iron Catalysts for Organic Pollutant Oxidation via Peroxymonosulfate Activation, *Environ. Sci. Technol.* 55 (2021) 8318–8328, <https://doi.org/10.1021/acs.est.1c01131>.
- [26] L. Ren, J. Liu, Y. Zhao, Y. Wang, X. Lu, M. Zhou, G. Zhang, W. Liu, H. Xu, X. Sun, Regulating Electronic Structure of Fe-N4 Single Atomic Catalyst via Neighboring Sulfur Doping for High Performance Lithium-Sulfur Batteries, *Adv. Funct. Mater.* 33 (2023), 2210509, <https://doi.org/10.1002/adfm.202210509>.
- [27] S. Ding, J.A. Barr, Z. Lyu, F. Zhang, M. Wang, P. Tieu, X. Li, M.H. Engelhard, Z. Feng, S.P. Beckman, X. Pan, J.-C. Li, D. Du, Y. Lin, Effect of Phosphorus Modulation in Iron Single-Atom Catalysts for Peroxidase Mimicking, *Adv. Mater.* n/a (2023), 2209633, <https://doi.org/10.1002/adma.202209633>.
- [28] Z. Zhou, M. Li, Y. Zhang, L. Kong, V.F. Smith, M. Zhang, A.J. Gulbrandson, G. H. Waller, F. Lin, X. Liu, D.P. Durkin, H. Chen, D. Shuai, Fe-Fe Double-Atom Catalysts for Murine Coronavirus Disinfection: Nonradical Activation of Peroxides and Mechanisms of Virus Inactivation, *Environ. Sci. Technol.* 57 (2023) 3804–3816, <https://doi.org/10.1021/acs.est.3c00163>.
- [29] C. Chen, M. Sun, F. Zhang, H. Li, M. Sun, P. Fang, T. Song, W. Chen, J. Dong, B. Rosen, P. Chen, B. Huang, Y. Li, Adjacent Fe Site boosts electrocatalytic oxygen evolution at Co site in single-atom-catalyst through a dual-metal-site design, *Energ. Environ. Sci.* 16 (2023) 1685–1696, <https://doi.org/10.1039/D2EE03930C>.
- [30] L. Fan, X. Wei, X. Li, Z. Liu, M. Li, S. Liu, Z. Kang, F. Dai, X. Lu, D. Sun, Phosphorus-doped iron-nitrogen-carbon catalyst with penta-coordinated single atom sites for efficient oxygen reduction, *Nano Res.* 16 (2023) 1810–1819, <https://doi.org/10.1007/s12274-022-4939-5>.
- [31] Y. Wang, J. Wu, S. Tang, J. Yang, C. Ye, J. Chen, Y. Lei, D. Wang, Synergistic Fe-Se Atom Pairs as Bifunctional Oxygen Electrocatalysts Boost Low-Temperature Rechargeable Zn-Air Battery, *Angew. Chem. Int. Ed.* 62 (2023), e202219191, <https://doi.org/10.1002/anie.202219191>.
- [32] K. Yin, R. Wu, Y. Shang, D. Chen, Z. Wu, X. Wang, B. Gao, X. Xu, Microenvironment modulation of cobalt single-atom catalysts for boosting both radical oxidation and electron-transfer process in Fenton-like system, *Appl. Catal. -B: Environ.* 329 (2023), 122558, <https://doi.org/10.1016/j.apcatb.2023.122558>.
- [33] Y. Gao, C. Yang, M. Zhou, C. He, S. Cao, Y. Long, S. Li, Y. Lin, P. Zhu, C. Cheng, Transition Metal and Metal-Nx Codoped MOF-Derived Fenton-Like Catalysts: A Comparative Study on Single Atoms and Nanoparticles, *Small* 16 (2020), 2005060, <https://doi.org/10.1002/sml.202005060>.
- [34] M.A. Nasir Khan, P.K. Klu, C. Xiao, M. Zhang, W. Zhang, Z. Sheikh, Y. Yang, Y. Zhou, Z. Zhu, J. Qi, J. Li, Hollow FeO/graphitized carbon nanocubes derived from the metal-organic framework for enhanced activation of peroxymonosulfate, *Sep. Purif. Technol.* 320 (2023), 124101, <https://doi.org/10.1016/j.seppur.2023.124101>.
- [35] Z. Zhang, H. Ding, Y. Li, J. Yu, L. Ding, Y. Kong, J. Ma, Nitrogen-doped biochar encapsulated Fe/Mn nanoparticles as cost-effective catalysts for heterogeneous activation of peroxymonosulfate towards the degradation of bisphenol-A: Mechanism insight and performance assessment, *Sep. Purif. Technol.* 283 (2022), 120136, <https://doi.org/10.1016/j.seppur.2021.120136>.
- [36] L. Peng, X. Duan, Y. Shang, B. Gao, X. Xu, Engineered carbon supported single iron atom sites and iron clusters from Fe-rich Enteromorpha for Fenton-like reactions via nonradical pathways, *Appl. Catal. -B: Environ.* 287 (2021), 119963, <https://doi.org/10.1016/j.apcatb.2021.119963>.
- [37] Q. Wang, Z. Xu, Y. Jiang, J. Lu, H. Li, X. Du, Z. Wang, Efficient peroxymonosulfate activation and less metallic leaching through kaolin@MnCo₂O₄ for bisphenol A degradation in environmental remediation, *Appl. Surf. Sci.* 585 (2022), 152705, <https://doi.org/10.1016/j.apsusc.2022.152705>.
- [38] Z.-Y. Guo, Y. Si, W.-Q. Xia, F. Wang, H.-Q. Liu, C. Yang, W.-J. Zhang, W.-W. Li, Electron delocalization triggers nonradical Fenton-like catalysis over spinel oxides, *Proc. Natl. Acad. Sci.* 119 (2022), e2201607119, <https://doi.org/10.1073/pnas.2201607119>.
- [39] X. Liu, H. Li, S. Gao, Z. Bai, J. Tian, Peroxymonosulfate activation by different iron sulfides for bisphenol-A degradation: Performance and mechanism, *Sep. Purif. Technol.* 289 (2022), 120751, <https://doi.org/10.1016/j.seppur.2022.120751>.

- [40] L. Yang, D. Xu, X. Luo, X. Zhu, J. Zhao, J. Song, Y. Han, G. Li, X. Gao, L. Liu, H. Liang, Fe(II)-Modulated Microporous Electrocatalytic Membranes for Organic Microcontaminant Oxidation and Fouling Control: Mechanisms of Regulating Electron Transport toward Enhanced Reactive Oxygen Species Activation, *Environ. Sci. Technol.* (2023), <https://doi.org/10.1021/acs.est.3c01792>.
- [41] Z. Yang, Y. Cui, B. Pan, J.J. Pignatello, Peroxymonosulfate Activation by Fe(III)-Picolinate Complexes for Efficient Water Treatment at Circumneutral pH: Fe(III)/Fe(IV) Cycle and Generation of Oxyl Radicals, *Environ. Sci. Technol.* (2023), <https://doi.org/10.1021/acs.est.3c00777>.
- [42] C. Nie, Y. Hou, F. Liu, Q. Dong, Z. Li, P. Han, M. Tong, Efficient peroxymonosulfate activation by magnetic $\text{MoS}_2/\text{Fe}_3\text{O}_4$ for rapid degradation of free DNA bases and antibiotic resistance genes, *Water Res.* 239 (2023), 120026, <https://doi.org/10.1016/j.watres.2023.120026>.
- [43] X. Zhou, R. Yin, J. Kang, Z. Li, Y. Pan, J. Bai, A.J. Li, R. Qiu, Atomic cation-vacancy modulated peroxymonosulfate nonradical oxidation of sulfamethoxazole via high-valent iron-oxo species, *Appl. Catal. -B: Environ.* 330 (2023), 122640, <https://doi.org/10.1016/j.apcatb.2023.122640>.
- [44] T. Liu, S. Xiao, N. Li, J. Chen, X. Zhou, Y. Qian, C.-H. Huang, Y. Zhang, Water decontamination via nonradical process by nanoconfined Fenton-like catalysts, *Nat. Commun.* 14 (2023), 2881, <https://doi.org/10.1038/s41467-023-38677-1>.
- [45] C. Cheng, W. Ren, F. Miao, X. Chen, X. Chen, H. Zhang, Generation of $\text{FeIV}=\text{O}$ and its Contribution to Fenton-Like Reactions on a Single-Atom Iron–N–C Catalyst, *Angew. Chem. Int. Ed.* 62 (2023), e202218510, <https://doi.org/10.1002/anie.202218510>.
- [46] Y. Wang, Z. Zhang, Z. Yin, Z. Liu, Y. Liu, Z. Yang, W. Yang, Adsorption and catalysis of peroxymonosulfate on carbocatalysts for phenol degradation: The role of pyrrolic-nitrogen, *Appl. Catal. -B: Environ.* 319 (2022), 121891, <https://doi.org/10.1016/j.apcatb.2022.121891>.
- [47] J. Miao, Y. Zhu, J. Lang, J. Zhang, S. Cheng, B. Zhou, L. Zhang, P.J.J. Alvarez, M. Long, Spin-State-Dependent Peroxymonosulfate Activation of Single-Atom M–N Moieties via a Radical-Free Pathway, *ACS Catal.* 11 (2021) 9569–9577, <https://doi.org/10.1021/acscatal.1c02031>.
- [48] L.-S. Zhang, X.-H. Jiang, Z.-A. Zhong, L. Tian, Q. Sun, Y.-T. Cui, X. Lu, J.-P. Zou, S.-L. Luo, Carbon Nitride Supported High-Loading Fe Single-Atom Catalyst for Activation of Peroxymonosulfate to Generate $^1\text{O}_2$ with 100% Selectivity, *Angew. Chem. Int. Ed.* 60 (2021) 21751–21755, <https://doi.org/10.1002/anie.202109488>.
- [49] Zhimin Jiang, Qiaoqing Zheng, Rongchen Shen, Peng Zhang, Xin Li, Constructing 1D/2D Schottky-Based Heterojunctions between $\text{Mn}_{0.2}\text{Cd}_{0.8}\text{S}$ Nanorods and Ti_3C_2 Nanosheets for Boosted Photocatalytic H_2 Evolution, *Acta Phys. -Chim. Sin.* 37 (2021) 2010059, <https://doi.org/10.3866/pku.Whxb202010059>.
- [50] Z. He, M. Chen, M. Xu, Y. Zhou, Y. Zhang, G. Hu, $\text{LaCo}_0.5\text{Ni}_{0.5}\text{O}_3$ perovskite for efficient sulfafurazole degradation via peroxymonosulfate activation: Catalytic mechanism of interfacial structure, *Appl. Catal. -B: Environ.* 335 (2023), 122883, <https://doi.org/10.1016/j.apcatb.2023.122883>.